

## Time and Space Resolved Heat Flux Measurements During Nucleate Boiling with Constant Heat Flux Boundary Conditions

Vamsee K. Yerramilli<sup>1</sup>, Jerry G. Myers<sup>2</sup>, Sam W. Hussey<sup>3</sup>  
Glenda F. Yee<sup>4</sup> and Jungho Kim<sup>5</sup>

1: Dept. of Mechanical Engineering, U. of Maryland, College Park, MD, 20742, vamsee@umd.edu

2: NASA Glenn Research Center, Brookpark, OH 44135, Jerry.G.Myers@grc.nasa.gov

3: NASA Glenn Research Center, Brookpark, OH 44135, Sam.W.Hussey@grc.nasa.gov

4: NASA Glenn Research Center, Brookpark, OH 44135, Glenda.F.Yee@grc.nasa.gov

5: Dept. of Mechanical Engineering, U. of Maryland, College Park, MD, 20742, kimjh@umd.edu

---

**Abstract** The lack of temporally and spatially resolved measurements under nucleate bubbles has complicated efforts to fully explain pool-boiling phenomena. The objective of this current work was to acquire time and space resolved temperature distributions under nucleating bubbles on a constant heat flux surface using a microheater array with  $100 \times 100 \mu\text{m}^2$  resolution, then numerically determine the wall to liquid heat flux. This data was then correlated with high speed ( $>1000\text{Hz}$ ) visual recordings of the bubble growth and departure from the heater surface acquired from below and from the side of the heater. The data indicate that microlayer evaporation and contact line heat transfer are not major heat transfer mechanisms for bubble growth. The dominant heat transfer mechanism appears to be transient conduction into the liquid as the liquid rewets the wall during the bubble departure process.

---

### 1. Introduction

Investigations into single bubble pool boiling phenomena are often complicated by the difficulties in obtaining time and space resolved information in the bubble region since the heaters and diagnostics used to measure heat transfer data are often on the order of, or larger than, the bubble characteristic length or region of influence. This has contributed to the development of many different and sometimes contradictory models of pool boiling phenomena and dominant heat transfer mechanisms. Mikic and Rosenhow [1] proposed a transient conduction model in which the departing bubble removed a portion of the superheated liquid layer twice the bubble departure diameter. Cold bulk liquid was assumed to rewet the surface immediately after bubble departure and transient conduction into this liquid occurred until nucleation of the next bubble. Cooper and Lloyd [2] measured wall temperature variations under bubbles using micro-thermocouples, and proposed that bubble heat transfer occurred through the formation and evaporation of a thin liquid layer (the microlayer) between the growing bubble and the wall. Stephan and Hammer [3] proposed that the heat transfer occurred primarily at the three-phase contact line where the liquid-vapor interface approaches the wall according to the mechanism proposed by Wayner et al. [4].

Yaddanapudi and Kim [5] measured local heat transfer underneath single bubbles nucleating periodically from a single site for saturated FC-72 at 1 atm ( $T_{\text{sat}}=56.7^\circ\text{C}$ ) and with the wall held at a constant wall temperature of  $79.2^\circ\text{C}$  using a microheater array with individual heaters  $270 \mu\text{m}$  in size. The bubble departure diameter was about  $370 \mu\text{m}$ , only slightly larger than a single heater. Their results indicated that bubble growth occurred primarily due to energy gained from the superheated liquid layer. Bubble departure resulted in rewetting of the wall by colder liquid, and heat transfer through transient conduction and/or microconvection, consistent with the model of Mikic and Rosenhow [1]. Demiray and Kim [6] presented local heat transfer data underneath bubbles nucleating from a single site for single and vertically merging bubbles under



conditions similar to Yaddanapuddi and Kim [5], but using an array with heaters 100  $\mu\text{m}$  in size. The surface temperature of the heater array and the bulk fluid temperature during the experiment were 76  $^{\circ}\text{C}$  and 52  $^{\circ}\text{C}$ , respectively. Bubbles that nucleated at this site alternated between two modes: single bubble mode and multiple bubble mode. In the single bubble mode, discrete bubbles departed from the heater array with a waiting time between the departure of one bubble and nucleation of the following bubble. In the multiple bubble mode, bubble nucleation was observed immediately after the previous bubble departed. The departing bubble pulled the growing bubble off the surface prematurely and the bubbles merged vertically forming small vapor columns. The data indicated that the area influenced by a single bubble departing the surface was approximately half the departure diameter. Microlayer evaporation was observed to contribute a significant, but not dominant, fraction of the wall heat transfer in the single bubble mode where a long waiting time preceded bubble nucleation. Microlayer evaporation was insignificant in the multiple bubble mode, and heat transfer occurred mainly through transient conduction and/or microconvection during liquid rewetting as the bubble departed the surface.

This study seeks to expand on the previous work by making time and space resolved measurements under bubbles nucleating on a microheater array operated under constant heat flux conditions. Wall temperature distributions were measured throughout the bubble nucleation and departure cycle using an array with microheaters 100  $\mu\text{m}$  in size, and were synchronized with high-speed videos. Wall heat transfer data was then obtained by numerically computing the heat lost to the substrate and subtracting this from the input heat. A description of the experimental setup, the results, and implications for modeling boiling heat transfer are presented.

## 2. Experimental Apparatus

### 2.1 Heater Array

The heater array in this experiment is similar to those used by Demiray and Kim [6]. The array consisted of 96 platinum resistance heaters microfabricated in a 10x10 configuration on a 500  $\mu\text{m}$  thick quartz wafer/substrate (Figure 1). After cleaning the as-received wafers, a 30 nm thick Ti adhesion layer was deposited onto the quartz followed by a 400 nm Pt layer. Standard photolithography was used to pattern the photoresist, and an ion mill was used to form the individual heaters followed by a plasma ash. Gold power leads 1  $\mu\text{m}$  thick were then deposited to allow connections to be made to the heaters.

Each array element was square with a nominal area of 0.01mm<sup>2</sup> and consisted of 2  $\mu\text{m}$  wide Pt lines spaced 2  $\mu\text{m}$  apart. Each heater exhibited a nominal resistance of 6 k $\Omega$  and a temperature coefficient of resistance of  $\sim 10 \Omega ^{\circ}\text{C}^{-1}$ . Gold lines that supply power to the heaters were routed between the heaters.

### 2.1 Control Circuit

Each heater was supplied with constant power by individual circuits consisting of a Wheatstone bridge and amplifier as shown on Figure 2.  $R_1$  was close to  $R_h$  in value, and was tailored for each circuit so that all heaters dissipated similar heat fluxes for a given  $V_{\text{top}}$  (voltage supplied to the bridge, See Figure 2). The ratio of  $R_2/R_3$  was similar to  $R_h/R_1$  at room temperature to minimize the offset voltage entering the amplifier. The analog output from each of the circuits was linearly proportional to  $V_{\text{heater}}$ . The heater power could be changed using  $V_{\text{top}}$ , and the heater current could be computed from

$$i_{\text{heater}} = \frac{V_{\text{top}} - V_{\text{heater}}}{R_1}$$

The power dissipated by a heater is  $q = i_{\text{heater}} V_{\text{heater}}$ . Although  $R_h$  increases as the heater temperature rises, the voltage across the heater  $V_{\text{heater}}$  also increases, resulting in a power dissipation that is



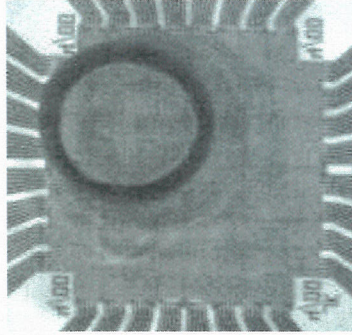


Figure 1: Photograph of heater array with single bubble nucleating on surface as seen from below the heater.

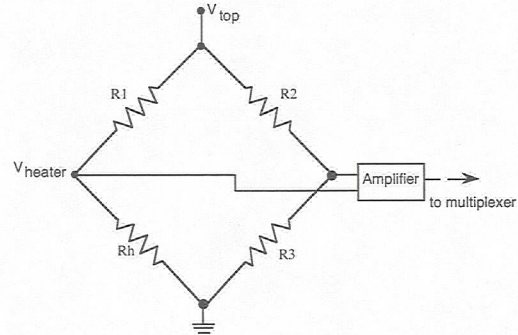


Figure 2: Circuit schematic for one heater.

essentially constant over the range of expected operating temperatures.

Twenty-four circuits were constructed on a single card, requiring 4 cards to control the array. All 4 cards are connected to a custom designed multiplexer board that controlled the  $V_{top}$  and acted as a router between the individual circuits and the computer/DAQ system.

### 2.1 Heater Calibration

Calibration of the heater array was performed using a two-step process. Initially the variation of heater resistance with temperature was determined by placing the array in an oven held to within  $0.1^\circ\text{C}$  of the set temperature and measuring the resistance of each heater over a range of temperatures from  $40^\circ\text{C}$  to  $100^\circ\text{C}$ . Two thermocouple attached to the underside of the heater assembly were used to ensure stability of the temperature environment.

The second step in the calibration involved calibrating the measured output voltage from each heater circuit (relative to the applied power) with the resistance of the heater. In this calibration step, the control boards and multiplexer were connected to banks of known resistors (nominally 6, 7 and  $8\text{ k}\Omega$ ). The output voltages and data acquisition readings of each heater circuit were then measured at each resistance level. Since an amplifier's output voltage was directly correlated to the resistance of a heater, this two-step process provided measurements of heater temperature with an expected uncertainty less than  $1^\circ\text{C}$ .

### 2.4 Boiling Rig

The boiling rig was custom designed and built at the NASA Glenn Research Center (Figure 3) to handle FC-72, which is used as the working fluid in this experiment. The boiling chamber was a rectangular  $9\times 9\times 14\text{ cm}$  aluminum chamber with a bellows pressure control system. The chamber incorporated three  $5\text{ cm}$  diameter view ports to allow optical access to the heater array. External surface mounted heaters (Thermofoil, Minco Products, Inc.) were attached to the chamber and covered by foam insulation to control the bulk fluid temperature. Fluid access ports were placed on one side of the chamber to allow mixing with an external pump if stratification was detected. Bulk fluid temperature was measured by two T-type thermocouples placed at different heights in the chamber. Chamber pressure was measured by an absolute pressure transducer ( $0\text{--}345\text{ kPa}$ ,  $\pm 0.4\text{ kPa}$ ) through an access port on one side of the chamber.

### 2.5 Data Acquisition and High Speed Video

A single data acquisition card (PCI-DIO96, Measurement Computing Corp.) capable of scanning 96 channels at  $200\text{ kHz}$  was installed in a Compaq Deskpro (Pentium III,  $667\text{ MHz}$ ) computer and



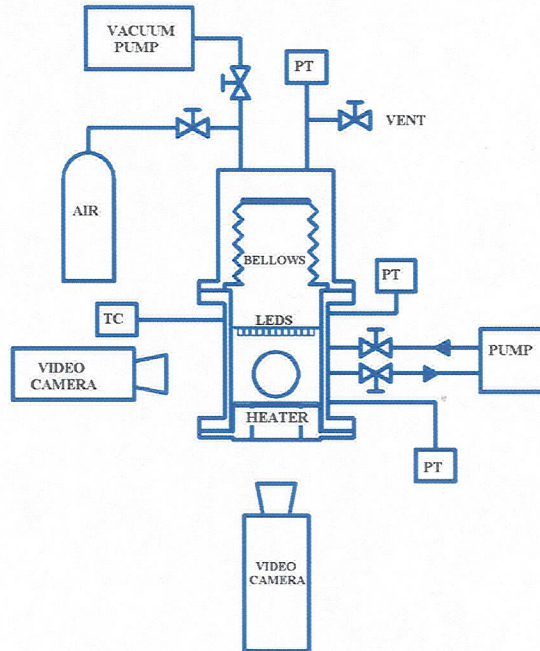


Figure 3: Illustration of custom designed boiling rig.

connected directly to the custom multiplexer board. Custom software, written in C, was created to control the experiment. The combined system was capable of obtaining time resolved temperature data from each heater at a rate of 1130 Hz for a set period of time (usually less than 20 seconds).

Temperature acquisition was synchronized with high-speed video acquisition. Because of the semi-transparent nature of the heater and substrate, it was possible to acquire images of the bubbles from below the boiling chamber using a high-speed camera (Vision Research Phantom IV) set to acquire 256x256 resolution images. Side view images of the bubbles were obtained (256x256 resolution) using a second high-speed camera (Vision Research Phantom V). Through the system multiplexer, the high-speed cameras were synchronized to acquire an image during the same rising edge TTL pulse from the computer. Two banks of high performance LED's provided the light for each camera view.

## 2.6 Imposed boundary condition

It should be noted that the boundary condition imposed on the bubble is not strictly constant wall heat flux because of the non-uniform substrate conduction across the heater array, and because 18 of the 96 heaters were non-functional (it is difficult to get all 96 heaters functioning when the line width is only 2  $\mu\text{m}$ ). The substrate conduction issue will be discussed in a future paper where it is accounted for. The non-functional heaters are difficult to account for, but the conclusions we will draw from the data do not seem to be affected by their presence.

## 3. Numerical Simulation

A three dimensional transient conduction simulation was used to determine the heat lost into the quartz substrate. The heat conduction equation was discretized using second order accurate discretization in spatial coordinates and fully implicit first order for temporal coordinates, and the resulting algebraic equations were solved using the Tri-Diagonal Matrix Algorithm (TDMA). The thermal conductivity (and specific heat) was assumed to be constant in the specified temperature range. There were no heat generation sources in the material. A 3-D finite difference model was



used with a linearly progressive grid along the  $z$  – direction (along the direction of thickness of the substrate). The substrate geometry (3mm x 3mm x 0.5 mm) was discretized using non-uniform grids along the  $x$ ,  $y$  and  $z$  directions. Along the length of 3mm of the substrate with the central 1mm being the heater area, 20 nodes were used each for the length and width of the heater and 10 nodes were used for the remaining 1mm on each side of the heater, resulting in a node distribution that was concentrated in the heater array region. Each heater had about 4 nodes with 2 along the  $x$  and  $y$  directions. Along the thickness of the substrate ( $z$ -direction) 20 nodes were used with a linearly progressive grid, having finest resolution close to the surface exposed to the liquid. The time step was about 0.000885 second (corresponding to 1130 Hz).

The temperature of each of the 96 heaters was recorded at a frequency of about 1130 Hz. This data was input to the program as a prescribed boundary condition for the top plane of the heater array. At every time step the temperature at every heater as imposed as a Dirichlet boundary condition while the remaining area of the substrate was assumed to experience a convective boundary condition with a bulk heat transfer coefficient of 200 W/m<sup>2</sup>K and the bulk fluid temperature at 52.7 °C. All other faces (the side walls and the bottom face of the substrate) were assumed to have adiabatic boundaries.

The results were checked for grid independence and this grid was found to be accurate for the current simulation. To simulate the 3-D transient case, we used a line-by-line TDMA with Gauss Seidel iteration combination to solve for the temperatures within the substrate. The convergence criteria stated that the error between successive iterations should be less than 0.01 %. The errors compared with steady state and transient analytical heat conduction models were found to be within 0.075% for 3-D steady state case and 1.5% for the 3-D transient case.

The algorithm solved for the temperatures at every point in the domain at every time step. Using this temperature distribution, the heat flux due to conduction loss into the quartz wafer at the top most layer was computed. Since the input heat flux to each of the heaters was known, the heat flux from the heater to the fluid above it (FC 72 liquid or vapor) can be computed by subtracting the conduction loss, enabling the heat flux to the fluid from the heater array to be computed at each time step. The digital images obtained during the experiment were colored using MATLAB based on this heat flux data.

## 4. Results

The boiling rig utilized distilled and degassed FC-72 as the working fluid. The voltage at the top of the bridge was initially set to be a high value ( $V_{top}$  between 8.7 V to 10 V) for 3.5 s to initiate nucleation on the surface, after which the voltage was dropped to the set value ( $V_{top}$ ) between 6.2 V to 8.3 V for 14.2 s. The bulk fluid temperature was 52.3 °C (+/-0.2 °C) and the dissipative heat flux ( $q''_{supplied}$ ) supplied to the array ranged from 14 to 25 W/cm<sup>2</sup>.

### 4.1 Wall temperature variations

The spatially averaged temperature of the middle 64 heaters vs. time is shown on Figure 4 for four representative voltages. Frame 0 corresponds to when the voltage drops to the set value, with each subsequent frame obtained 0.000885s from the last (1130 Hz acquisition rate). All of the heater temperatures initially decay as a result of the drop in voltage, but then approach a steady value. Visual observation of the boiling behavior indicated that only a single bubble was observed on the surface when  $V_{top}$  was 6.8 V and lower. For the 6.2 V case, nucleation ceased altogether beginning from frame 1450, resulting in an increase in the wall temperature as the wall adjusts to the natural convection above the heater. Oscillations in the temperature are seen when bubbles are



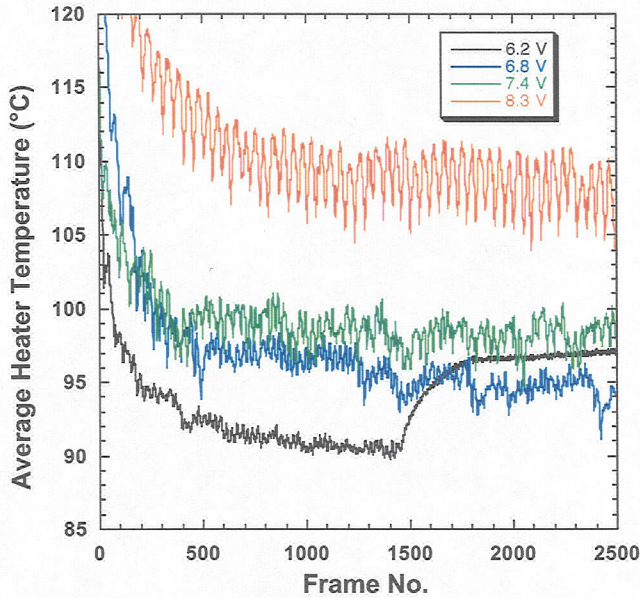


Figure 4: Average heater temperatures (middle 64 heaters) vs. time. Each frame represents 0.000885s.

present on the surface. Multiple bubbles were observed to coexist on the surface when the voltage was 7.1 V and higher. For the 8.3 V case, multiple satellite bubbles surrounding a single large bubble and merging with it were observed.

Images of bubbles on the surface during one bubble nucleation and departure cycle for  $V_{\text{top}}=6.8$  V are shown on Figure 5. Images (frames 825-859) of a bubble nucleation and departure event for the 6.8 V case are shown on Figure 6 where every other frame of the high-speed video is presented. Each of the heaters has been colored according to its temperature. Non-functional heaters are not colored. The dark rings that are clearly visible in the images result from shadows cast by the growing bubble. It can be shown from simply ray tracing (see Yin et al. [7]) that the outer diameter of this ring corresponds to the diameter of the bubble while the thickness of the ring depends on the bubble shape. A thin ring means the bubble shape is close to being hemispherical. Thicker rings result from a more spherical bubble. The inside diameter of the ring can also be a measure of the dry spot size.

Departure of a bubble is observed in Frames 825-831. The outer diameter of the ring remains roughly constant while the inner diameter decreases, indicating rewetting of the dry spot by liquid as the bubble pulls off the surface. Nucleation of a new bubble and its rapid growth are observed in Frames 833-839. The images show that the bubble grows hemispherically through Frame 841, as indicated by the thin, dark ring, to a maximum diameter of about 900 microns. The bubble takes about 7 ms to reach this size from nucleation—this is significantly slower than was observed for a similar bubble growing on a constant temperature surface for which it took less than 2 ms to reach its maximum size [6]. It is believed that a dry spot forms on the wall under the bubble during this time. The bubble then becomes progressively more spherical as indicated by the thickening of the ring, during which liquid rewets the surface. Bubble departure occurs at Frame 859 after which a new bubble immediately nucleates and grows.

The heater temperatures under the growing bubble do not decrease during initial hemispherical bubble growth (frames 833-839), implying that the energy for bubble growth could not have come from the wall, and must have come from the superheated liquid layer. The heaters under the bubble increase in temperature once a dry spot forms since power is continually supplied to them while little energy is removed by the low thermal conductivity vapor (frames 841-849). These same heaters are observed to decrease in temperature as they are rewet by liquid as the bubble departs the surface (frames 851-859).



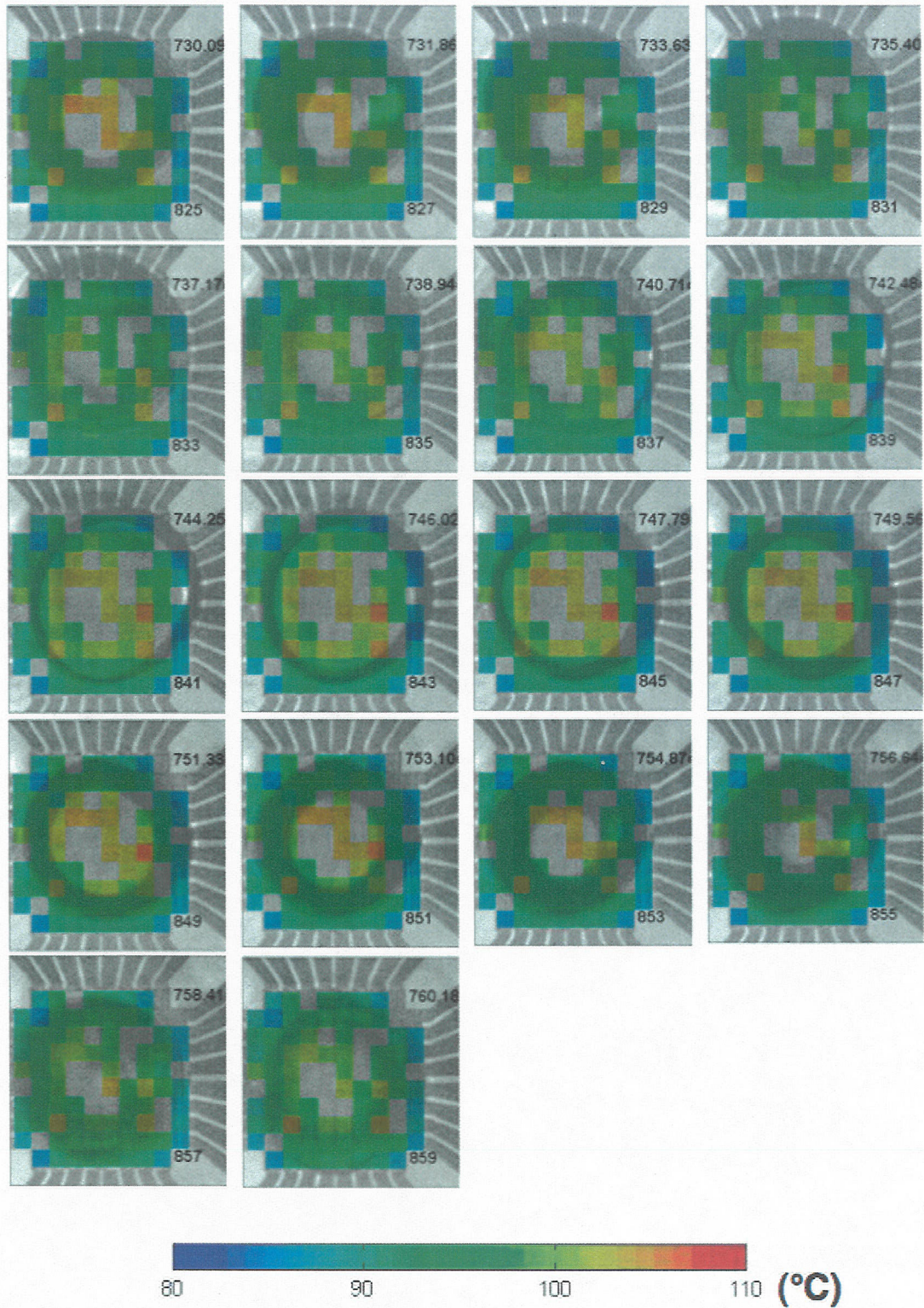


Figure 5: Surface temperature distribution through one bubble nucleation and departure cycle at 6.8 V. The time and frame numbers are given in the upper right and bottom right respectively of each frame.



#### 4.2 Wall heat flux variations

Some very preliminary wall heat flux data obtained using the procedure described in section 3 is shown below for a voltage of 6.8 V. This data is believed to be reliable for determining relative changes in heat flux across the array, but the data is *not* a reliable measure of the absolute heat flux. The problem stems from the numerical calculation of the substrate conduction. The extent of the domain around each side of the array in the calculation was limited to 1 mm due to time constraints, but this was found to result in wall temperatures at the edge of the domain that were much higher than the bulk liquid temperature. The calculated values of substrate conduction were much too low as a result, shifting the heat flux values to be discussed below significantly upward. Calculations are currently being performed over a much larger domain, and the results with correct values of substrate conduction will be reported in the future.

Heat flux distributions corresponding to the time resolved temperatures are shown on Figure 5. Frames 831-839 indicate that the heat transfer *decreases* as the bubble nucleates and grows on the surface. As mentioned earlier, dryout is believed to occur on the surface. The heat transfer should be very low on the center heaters at this time since heat loss occurs by conduction into vapor—the high heat transfer indicated is thought to be a result of the incorrect estimation of substrate conduction. Once the bubble departure process begins and liquid rewets the surface, the heat transfer from the heaters under the advancing contact line increases, and the peak array heat flux occurs around frame 855 just before the bubble actually departs. These results are consistent with the observations obtained by Yaddanapuddi and Kim (5) and Demiray and Kim (6) with the heaters operated in constant wall temperature mode.

The temporal variation in the spatially averaged heat flux over the middle 64 heaters is shown on Figure 7. Over a bubble departure cycle, the heat flux peaks as the bubble departs. The heat flux decreases as the bubble grows and reaches a minimum around the time the dry area under the bubble reaches its maximum extent. The heat flux then increases as liquid rewets the surface during bubble departure. The variations in the space averaged heat flux are only about 1 W/cm<sup>2</sup>. Much larger variations occur locally. Heat fluxes averaged over “rings” of heaters are shown on Figure 8. The outer ring of heaters (heaters 37-64) experience mostly natural convection, but increases on the order of 0.6 W/cm<sup>2</sup> are seen when the advancing contact line passes over them as the bubble begins to depart. Similarly, heaters 17-36 experience increases of about 1.4 W/cm<sup>2</sup> while the center 16 heaters experience heat flux variations of about 2 W/cm<sup>2</sup>. It has been shown by Demiray and Kim (6) that the heat transfer under an advancing contact line is proportional to the velocity with which it advances. To check this, measurements of the dry spot diameter vs. time were obtained from the images, and the velocity of rewetting was calculated. The results shown on Figure 9 indicate that the rewetting velocity increases during the bubble departure process and reaches a maximum just as the bubble departs, consistent with the increases in heat transfer.

Yaddanapuddi and Kim (5) and Demiray and Kim (6) integrated the energy from the wall over the bubble growth period and concluded that the wall heat transfer with constant wall temperature boundary condition could not account for the energy required to grow a bubble of the observed size. They found that the energy to produce the bubble was transferred into the superheated liquid layer by transient conduction during the waiting time between bubble departure events. It appears that similar conclusions can be made for boiling on surfaces with constant wall heat flux boundary condition, but calculations will be performed once correct substrate conduction values are obtained to verify this.

In summary, the results described above are not consistent with a microlayer evaporation dominated boiling heat transfer mechanism, which predicts large heat transfer rates during bubble growth just after nucleation. We observed the heat transfer to decrease after nucleation indicating that the bubble growth and the wall heat transfer are not correlated. The results are also not consistent with contact line heat transfer dominated boiling. It would be expected from contact line theory that the heat transfer as the bubble grows (receding contact line and smaller contact angles) would be higher than



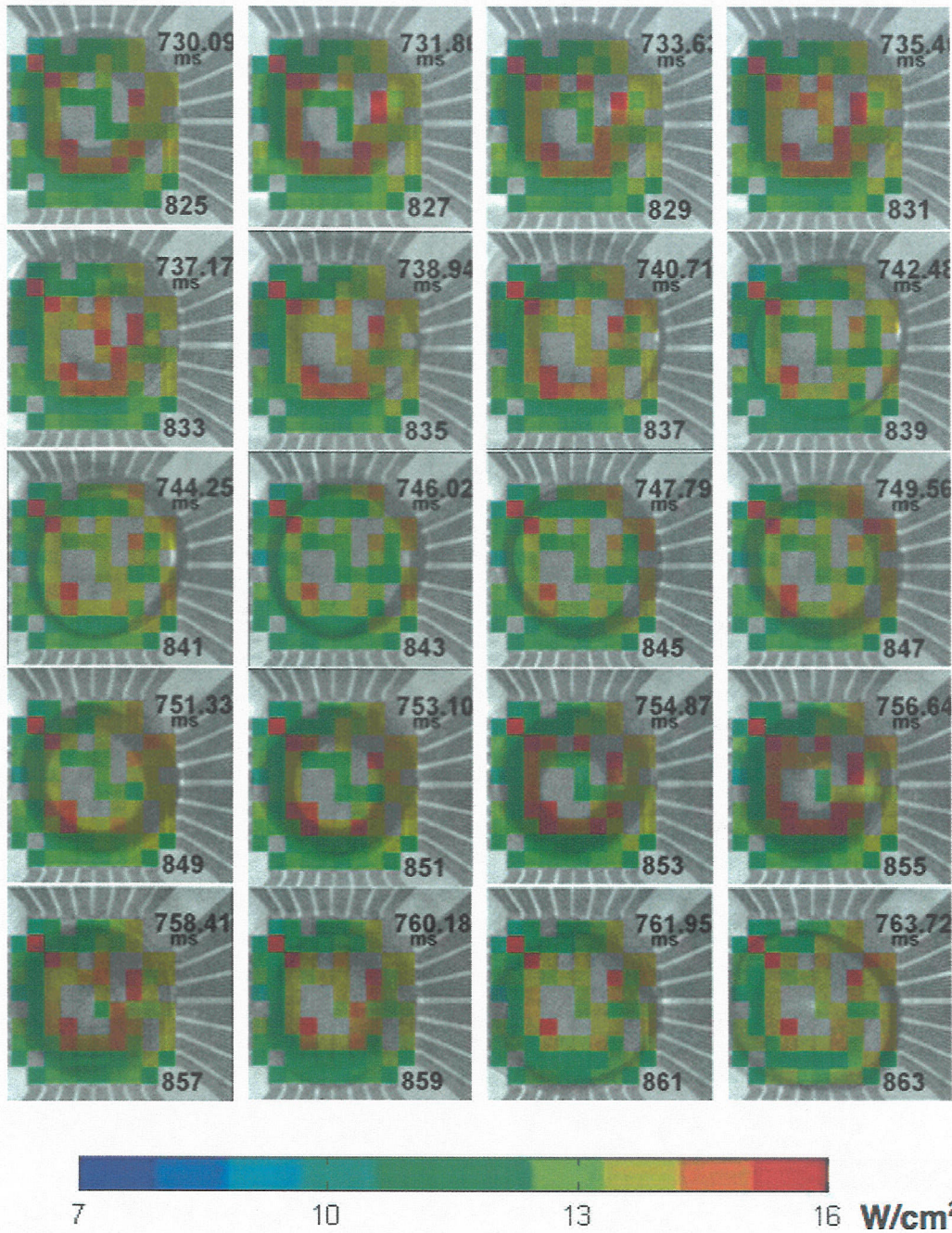


Figure 6: Preliminary surface heat flux distribution through one bubble nucleation and departure cycle at 6.8 V. The time and frame numbers are given in the upper right and bottom right respectively of each frame.



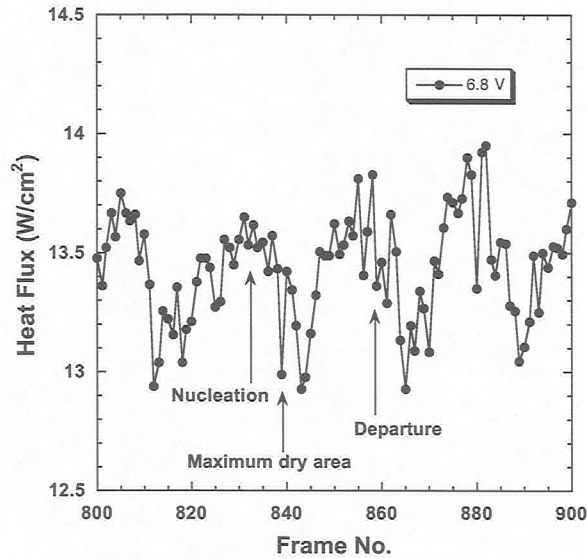


Figure 7: Preliminary space averaged, time resolved heat flux from the middle 64 heaters.

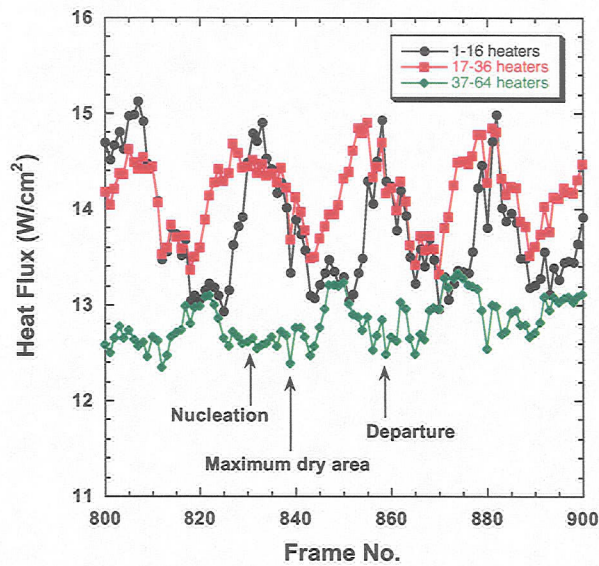


Figure 8: Preliminary space resolved wall heat flux variation. Heater 1-16 are the central 4x4 heaters, and heaters 17-36 and 37-64 are “rings” of heaters in the radial direction.

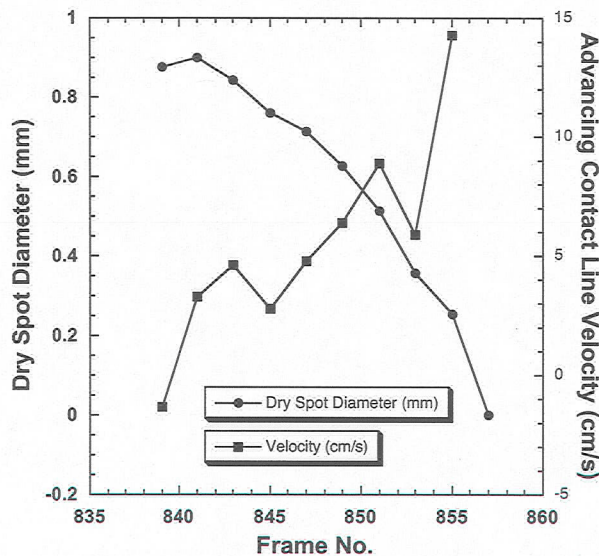


Figure 9: Dry spot diameter and advancing contact line velocity for a single bubble.



when the bubble departs (advancing contact line and larger contact angles) if liquid flow to the meniscus were not limited, but this is also not observed. Since the heat transfer increases as the bubble departs, transient conduction into the rewetting liquid appears to be the dominant heat transfer mode.

## 5. Conclusions

Time and space resolved temperature measurements, correlated to high-speed images of bubble nucleation, growth and release in FC-72, were obtained using a microheater array consisting of 96  $100 \times 100 \mu\text{m}^2$  heaters operated with a constant heat flux. Preliminary heat fluxes from the wall to the liquid were numerically obtained. The data indicate that microlayer evaporation and contact line heat transfer are not major heat transfer mechanisms for bubble growth. The dominant heat transfer mechanism appears to be transient conduction into the liquid as the liquid rewets the wall during the bubble departure process.

## References

1. Mikic, B.B. and Rosenhow, W.M. (1969), "Bubble growth rates in non-uniform temperature field", Prog. in Heat and Mass Transfer, Vol. II, pp. 283-292.
2. Cooper, M.G. and Lloyd, A.J.P. (1969), "The microlayer in nucleate boiling", Int. J. of Heat and Mass Transfer, Vol. 12, pp. 895-913.
3. Stephan, P. and Hammer, J. (1995), "New Model for Nucleate Boiling Heat Transfer", Heat and Mass Transfer/Waerme-und Stoffuebertragung, Vol 30, No. 2, p 119-125.
4. Wayner, P.C., Kao, Y.K. and LaCroix, L.V. (1976), Int. J. Heat Mass Transfer, Vol. 19 (1976) 487.
5. Yaddanapudi, N., and Kim, J., "Single Bubble Heat Transfer in Saturated Pool Boiling of FC-72", Multiphase Science and Technology, Vol. 12, No. 3-4, pp. 47-63, 2001.
6. Demiray, F. and Kim, J., "Microscale Heat Transfer Measurements During Pool Boiling of FC-72: Effect of Subcooling", International Journal of Heat and Mass Transfer, in press.
7. Yin, Z., Prosperetti, A., Kim, J. "Bubble Growth on an Impulsively Powered Microheater", International Journal of Heat and Mass Transfer, Vol. 47, No. 5, pp. 1053-1067, 2004.